*Progress In Electromagnetics Research C, Vol. 121, 179–195, 2022*

# Optimal Duty Cycle Model Predictive Current Control Based on Internal Model Observer for PMSM

**Dingdou Wen, Yanqin Zhang, and Yang Zhang***

**Abstract**—This paper presents an optimal duty cycle model predictive current control (ODC-MPCC) strategy based on the internal model observer (IMO) for permanent magnet synchronous motor (PMSM). First, in order to be able to control the current quickly and better, the partial derivative of the cost function with respect to the optimal duty cycle is directly used. On this basis, a five-segment algorithm is used to allocate the optimal duty cycle and output voltage with arbitrary amplitude and direction. In addition, to reduce the current static error under parameter mismatch, the IMO is designed to estimate the system disturbance caused by parameters variation which is used for feedforward compensation. Finally, experiments show that the proposed method can effectively reduce the current ripple and static error and improve the steady-state performance of the system.

## 1. INTRODUCTION

Permanent magnet synchronous motor has the advantages of light weight, small size, and high power density, and is now widely used in drive systems such as new energy drives, electric vehicles, and aerospace [1].

With the improvement of the performance of digital processing chips, the application of Model Predictive Control (MPC) has become a research hotspot [2, 3]. According to different control objects, MPC can be divided into model predictive torque control and MPCC. Conventional MPCC directly selects the switching signal of the inverter through the cost function, without any modulation link, with simple control algorithm and fast dynamic response [4]. However, in conventional MPCC, the amplitude and phase of the output voltage vector are constant, and there are problems such as unstable switching frequency and large current ripple [5]. To address the problems of conventional MPCC, many scholars use zero vector to adjust the amplitude of active voltage vector, but the direction of the synthesized voltage vector remains unchanged, and the current ripple is large [6]. In [7], for the problem in [6], the second voltage vector is no longer limited to zero vector. The strategy loses zero vector regulation amplitude, and steady-state performance is not improved. Based on [6, 7], a three-vector model predictive current control strategy is proposed [8]. Combining the two active voltage vectors and zero vector, the output voltage can cover any amplitude and direction, effectively reducing the current ripple and improving steady-state performance. However, the above methods all calculate the current slope first and then calculate the action time based on the deadbeat principle. Therefore, the calculation amount is large, and the problem of large static current error caused by parameter mismatch is also not considered.

PMSM is a nonlinear and strongly coupled system. The motor parameters vary with temperature rise and magnetic saturation, and the change of the motor parameters leads to degradation of control system performance [9]. To address the shortcomings of parameter mismatch affecting control performance, scholars have conducted a series of researches [10–17]. Compensating the disturbance

*Received 29 April 2022, Accepted 22 June 2022, Scheduled 19 July 2022*
* Corresponding author: Yang Zhang (459387623@qq.com).
The authors are with the College of Electrical and Information Engineering, Hunan University of Technology, Zhuzhou 412007, China.

estimated by the sliding mode observer into the speed loop improves the response speed and anti-interference ability, which does not consider the effect of the disturbance on the current loop [10]. To improve the quality of the current loop, methods such as adaptive observer [11], nonlinear disturbance observer [12], extended state observer [13], and Luenberger observer [14] are used to estimate system disturbances and feed forward and compensate them to the current loop, improving the steady-state performance of the control system. In [15], a control strategy combining sliding mode controller and disturbance observer is proposed. The sliding mode variable structure control is model independent and has strong nonlinearity and robustness, but the introduction of sliding mode control causes certain current jitter. In [16], a model-aided active disturbance rejection control (ADRC) algorithm based on online parameter identification is proposed. The algorithm can provide accurate identification values for the model, but the parameters of ADRC are difficult to be determined. In [17], a robust model prediction scheme is proposed. By extending the voltage vector, the accuracy of the predicted current is improved, but the calculation burden is large. In [18], an online inductance correction method is proposed to reduce the current prediction error of PMSM, but it has limitations by not considering the flux linkage and resistance mismatch. Aiming the problem that deadbeat predictive current control (DPCC) relies on the motor mathematical model, a current static error elimination algorithm is introduced to improve the robustness of DPCC. It cannot actually eliminate the current static error in [19]. On the other hand, DPCC directly outputs the voltage signal to the space vector modulation link, which does not take advantage of MPCC direct selection of the optimal voltage vector and duty cycle through the cost function, resulting in a certain switching tube loss.

Due to the advantages of simple structure and few adjustment parameters, internal mode control (IMC) has been widely used in the field of PMSM [20]. In the PMSM speed control system, an adaptive internal mode controller is designed to automatically adjust the parameters of the speed control controller [21]. However, establishing fuzzy adaptive laws requires a priori experimental test and experience. In [22, 23], an IMO was designed to estimate the parameter perturbation, compensate the current loop, and reduce the current static error under the parameter perturbation. In this paper, a current loop observer is designed using an IMO to achieve disturbance compensation, so as to suppress the adverse effects of motor parameter variations on the control system.

To address the above problems, an ODC-MPCC strategy based on IMO is proposed. For direct prediction of the voltage vector, the predicted current is transformed equivalently. Among the six active voltage vectors output by the two-level inverter, only active voltage vector with a spatial difference of 120° is used, which is called phase voltage vector. In order to take full advantage of the cost function, the partial derivative of the cost function with respect to the duty cycle is creatively calculated, and the optimal duty cycle of each phase voltage vector is obtained directly. Using the five-segment algorithm to assign the optimal duty cycle, voltage with arbitrary amplitude and direction is output. Compared with Dual Vector Model Predictive Current Control (DV-MPCC), the current ripple is significantly reduced. The proposed strategy has only 3 predictions compared to 6 predictions of DV-MPCC. To further improve the adaptability of ODC-MPCC to parameters variation, IMO is designed to estimate disturbance and compensate the voltage equation with feedforward. Finally, the experimental results verify the reliability and effectiveness of this method.

## 2. MATHEMATICAL MODEL OF PMSM

Assumptions, ignoring core saturation, eddy current and core loss, the conductivity of permanent magnet material is zero; there is no resistance winding on the rotor; and the induced electromotive force in the phase winding is a sine wave.

In the synchronous rotating coordinate system, the voltage equation of surface PMSM is expressed as:

$$\begin{cases} u_d = R_s i_d + L_s \dfrac{di_d}{dt} - \omega_e L_s i_q \\ u_q = R_s i_q + L_s \dfrac{di_q}{dt} + \omega_e L_s i_d + \omega_e \psi_f \end{cases} \tag{1}$$

where $u_d$ and $u_q$ are the $d$-$q$ axis stator voltage components, respectively. $i_d$ and $i_q$ are the $d$-$q$ axis stator current components, respectively. $R_s$, $L_s$, $\psi_f$, and $\omega_e$ denote stator resistance, stator inductance,

permanent magnet flux linkage, and electrical angular velocity, respectively.

For Equation (1), forward Euler discretization is adopted to obtain:

$$\begin{cases} i_d(k+1) = i_d(k) + \dfrac{T_s}{L_s}\left(u_d(k) - R_s i_d(k) + e_d(k)\right) \\ i_q(k+1) = i_q(k) + \dfrac{T_s}{L_s}\left(u_q(k) - R_s i_q(k) + e_q(k)\right) \end{cases} \tag{2}$$

$$\begin{cases} e_d(k) = \omega_e(k) L_s i_q \\ e_q(k) = -\omega_e(k) L_s i_d - \omega_e(k)\psi_f \end{cases} \tag{3}$$

where $u_d(k)$ and $u_q(k)$ are the $d$-$q$ axis voltage components at the constant $k$, respectively. $i_d(k+1)$ and $i_q(k+1)$ are the $d$-$q$ axis current components at the constant $k+1$, respectively. $i_d(k)$ and $i_q(k)$ are the $d$-$q$ axis current components at the constant $k$, respectively. $\omega_e(k)$ is the electrical angular velocity at the constant $k$. $e_d(k)$ and $e_q(k)$ are the $d$-$q$ axis back EMF at the constant $k$, respectively. $T_s$ is the sampling time.

## 3. DESIGN OF DV-MPCC CONTROLLER

The principle of DV-MPCC is to use an active voltage vector and a zero vector in one sampling period, because zero vector can only adjust the amplitude of the active voltage vector, so the synthetic voltage vector remains on the axis of the active voltage vector. The synthetic voltage vector is shown in Fig. 1.

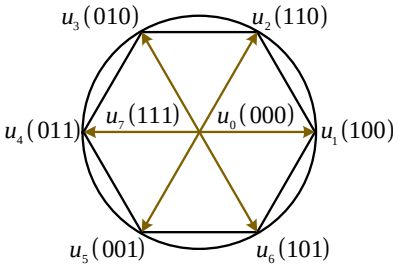


**Figure 1.** DV-MPCC synthetic voltage vector diagram.

In this paper, the control method of $i_d^* = 0$ is used. The speed loop adopts PI control and outputs the reference value of $i_q$. The design steps of the DV-MPCC control strategy are as follows. First, the reference voltage vector is calculated. Then, the duty cycle of active voltage vectors is obtained by deriving the cost function. Finally, the optimal active voltage vector and duty cycle are selected by the cost function to generate a pulse signal and act on the inverter. The block diagram of the control system is shown in Fig. 2.

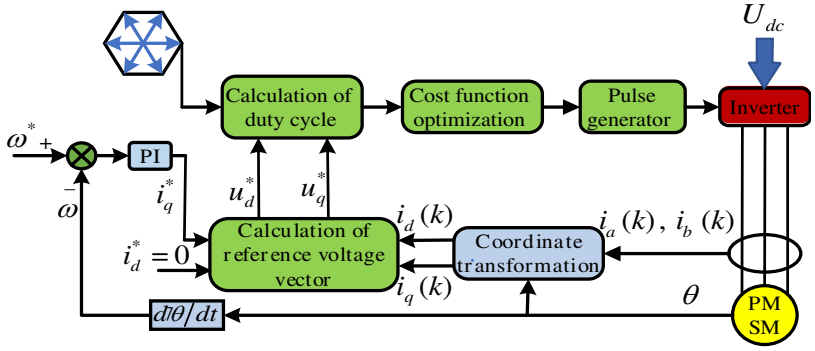


**Figure 2.** Structure block diagram of DV-MPCC.

Rewrite (2) as follows:

$$i_s(k+1) = i_{s0}(k) + \frac{T_s}{L_s} u_s(k) \tag{4}$$

$$i_{s0}(k) = \frac{(L_s - T_s R_s) i_s(k) + T_s E(k)}{L_s} \tag{5}$$

where

$$\begin{cases} i_s(k+1) = [\ i_d(k+1) \quad i_q(k+1)\ ]^{\mathrm{T}} \\ i_s(k) = [\ i_d(k) \quad i_q(k)\ ]^{\mathrm{T}} \\ u_s(k) = [\ u_d(k) \quad u_q(k)\ ]^{\mathrm{T}} \\ E(k) = [\ e_d(k) \quad e_q(k)\ ]^{\mathrm{T}} \end{cases}$$

According to the deadbeat principle, the predicted current at the constant $(k+1)$ is equal to the current reference, i.e., $i_s(k+1) = i_s^*$, and substitute (4) to obtain the reference voltage at the current moment, as follows:

$$u_s^* = \frac{L_s}{T_s}(i_s^* - i_{s0}(k)) \tag{6}$$

where $u_s^* = [\ u_d^* \quad u_q^*\ ]^{\mathrm{T}}$.

According to (4) and (6), based on the deadbeat principle, the cost function can be equivalently constructed as:

$$g = (u_s^* - u_s(k+1))^2 \tag{7}$$

From (7), it can be known that the tracking error of the minimum current can be converted into the tracking error of the minimum voltage. The chosen vector is equivalent to the traditional method of predicting current. However, it is no longer necessary to indirectly select the voltage vector of the inverter by predicting the current. Thus, the computational effort is small [24].

The *d*-*q* axis component of the DV-MPCC synthetic voltage vector is expressed as:

$$\begin{cases} u_d(k+1) = \gamma_j u_{dj} \\ u_q(k+1) = \gamma_j u_{qj} \end{cases} \tag{8}$$

where $u_{dj}$ and $u_{qj}$ are the components of active voltage vector on the *d*-*q* axis, and $\gamma_j$ is the duty cycle of active voltage vector, $j = 1, 2, 3, 4, 5, 6$.

Substituting (8) into (7), with the derivative of the cost function with respect to $\gamma_j$ and letting $dg/d\gamma_j = 0$, the duty cycle can be obtained as:

$$\gamma_j = \frac{u_{dj} u_d^* + u_{qj} u_q^*}{u_{dj}^2 + u_{qj}^2} \tag{9}$$

After the duty cycle of active voltage vector is calculated by (9), it is substituted into (8) to predict the voltage at the next moment. The optimal active voltage vector and duty cycle are selected by the cost function (7), and the driving signal is generated to act on the inverter.

## 4. DESIGN OF ODC-MPCC METHOD BASED ON IMO CONTROLLER

The ODC-MPCC strategy based on IMO consists of five parts: calculation of reference voltage vector, calculation of duty cycle, IMO, cost function optimization, and duty cycle assignment. Its structure diagram is shown in the filled area of Fig. 3.

### 4.1. Calculation of Duty Cycle and Optimization of Cost Function

The two-level inverter has eight switching states. If the switching state $S_{abc} = 100, 010, 001$ is selected, the voltage vector with a spatial difference of 120° divides the entire hexagon into three sectors, and the sectors is shown in Fig. 4. In Fig. 4, when the reference voltage $u_s$ falls in sector I, it can be obtained by synthesizing $u_1$, $u_3$ and zero vector. By analogy, when the reference voltage vector falls in any region of

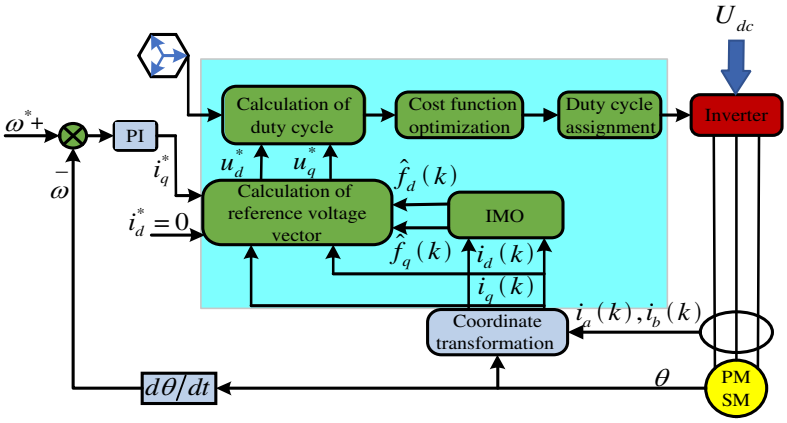


**Figure 3.** Structure block diagram of ODC-MPCC based on IMO.

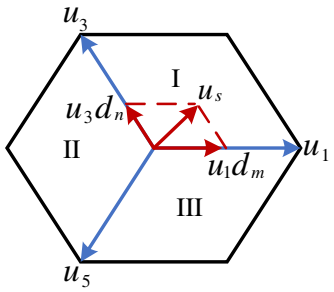


**Figure 4.** Schematic diagram of phase voltage vector distribution and resultant voltage.

the positive hexagon, it can be obtained by the synthesis of phase voltage vector and zero vector [25]. The reference voltage vector is located in different sectors and synthesized by different phase voltage vectors and corresponding duty cycles. The relationship between the reference voltage vector and phase voltage vector is shown in Table 1, and the synthetic voltage vector is expressed as (10).

$$u_s = u_m d_m + u_n d_n \tag{10}$$

where $u_m$ and $u_n$ are the phase voltage vectors, and their duty cycles are $d_m$ and $d_n$, respectively. $d_m,\ d_n \in [\ 0 \quad 1\ ]$.

**Table 1.** Relationship between sector and effective phase voltage vector.

| sector | $u_m$ | $u_n$ |
|---|---|---|
| I | $u_1$ | $u_3$ |
| II | $u_3$ | $u_5$ |
| III | $u_5$ | $u_1$ |

The components of the synthetic voltage vector on the $d$ and $q$ axes are expressed as follows:

$$\begin{cases} u_d(k+1) = u_{mdi} d_{mi} + u_{ndi} d_{ni} & i = 1, 2, 3 \\ u_q(k+1) = u_{mqi} d_{mi} + u_{nqi} d_{ni} & i = 1, 2, 3 \end{cases} \tag{11}$$

where $u_{mdi}$ and $u_{ndi}$ are the components of phase voltage vector of the $i$-th sector on the $d$-axis; $u_{mqi}$ and $u_{nqi}$ are the components of phase voltage vector of the $i$-th sector on the $q$-axis; $d_{mi}$ and $d_{ni}$ are the duty cycle of phase voltage vector of the $i$-th sector.

Substituting (11) into (7), $d_{mi}$ and $d_{ni}$ can be obtained by first-order partial derivatives. Let $\partial g/\partial d_{mi} = 0$, $\partial g/\partial d_{ni} = 0$, the duty cycle of phase voltage vector can be obtained as follows:

$$\begin{cases} d_{mi} = \dfrac{CB - DE}{F} \\ d_{ni} = \dfrac{AD - CE}{F} \end{cases} \tag{12}$$

where

$$\begin{cases} A = u_{mdi}^2 + u_{mqi}^2 \\ B = u_{ndi}^2 + u_{nqi}^2 \\ C = u_{mdi}u_d^* + u_{mqi}u_q^* \\ D = u_{ndi}u_d^* + u_{nqi}u_q^* \\ E = u_{mdi}u_{ndi} + u_{mqi}u_{nqi} \\ F = (u_{mdi}u_{nqi} - u_{mqi}u_{ndi})^2 \end{cases}$$

When the speed or load of the motor suddenly changes, the calculated duty cycle may not be within the valid range [0 1], so it is necessary to correct the calculated duty cycle, and the possible cases are as follows:

(1) If the duty cycle of phase voltage vector is less than 0, the phase voltage vector is cancelled.

(2) If the duty cycle of phase voltage is greater than 1, in order to ensure that the ratio of the duty cycle remains unchanged, the correction formula is as follows:

$$\begin{cases} d_{mi} = d_{ni}/d_{mi}, \quad d_{ni} = 1 \quad d_{mi} \le d_{ni} \\ d_{ni} = d_{mi}/d_{ni}, \quad d_{mi} = 1 \quad d_{mi} > d_{ni} \end{cases} \tag{13}$$

The corrected duty cycle is substituted into (14) to obtain the predicted voltage value, and then the predicted voltage value is substituted into (11). The phase voltage vector $u_{md} = u_{mdk}$, $u_{md} = u_{mdk}$ and duty cycle $d_m = d_{mk}$, $d_n = d_{nk}$ that minimize the cost function are chosen as optimal combination, where $k = 1, 2, 3$ represents the number of sectors.

The number of sectors and the corresponding duty cycle of phase voltage vector are obtained above and need to be further optimized before outputting the drive pulse to achieve better control effect. The boundary vectors of the three sectors are all single-phase voltage vectors, independent of each other, and the original three-phase duty is shown in Fig. 5. According to the SVPWM principle, the action times of the three-phase vectors can overlap each other, so the duty cycle of zero vector can be determined by Equation (14).

$$\begin{cases} d_0 = 1 - d_n \quad d_m \le d_n \\ d_0 = 1 - d_m \quad d_m > d_n \end{cases} \tag{14}$$

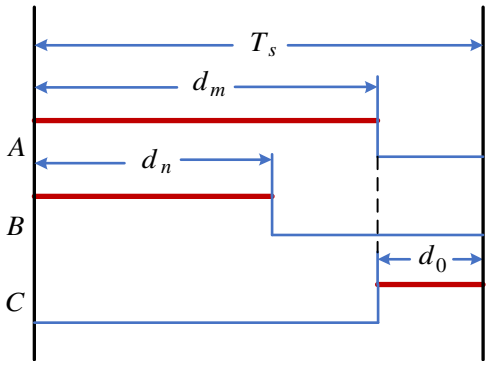


**Figure 5.** Original three-phase pulse schematic.

### 4.2. Duty Cycle Assignment

In order to reduce the loss of the switch tube as much as possible, a five-segment algorithm is used to assign the duty cycle, and the action time of the zero vector is the action time of $u_7(111)$. Fig. 6 shows the three-phase pulse waveforms of the three sectors. The following is a brief description of the three-phase duty cycle. In sector I, the duty cycle $d_m$ of $u_1$, the duty cycle $d_n$ of $u_3$, and the duty cycle $d_0$ and $d_c$ are three-phase duty cycles of A, B, and C, respectively. The analysis of other sectors is consistent with the above principles and will not be repeated here.

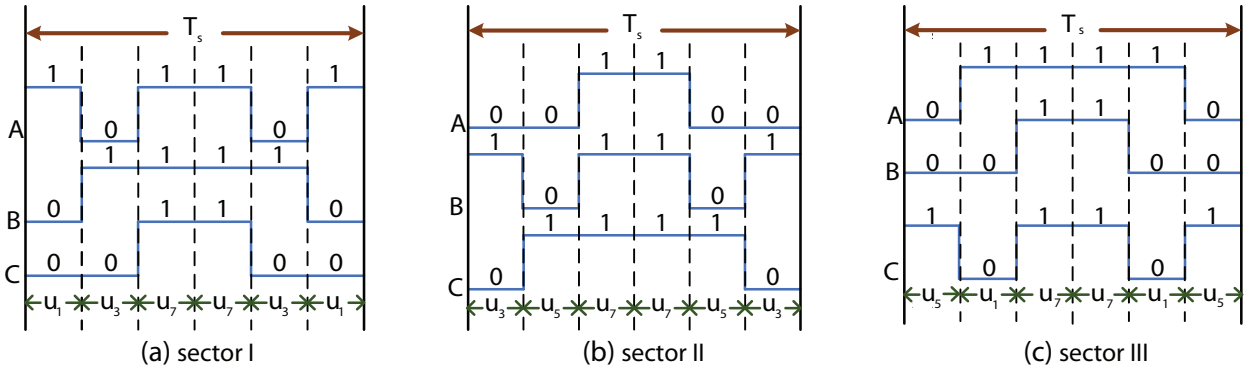


**Figure 6.** Three-phase pulse signal.

According to the minimization of the cost function, the duty cycle corresponding to phase voltage vector is assigned, and the duty cycle is defined as (15). The assignment results are shown in Table 2.

$$\begin{cases} d_x = d_m + d_0 \\ d_y = d_n + d_0 \\ d_z = d_0 \end{cases} \tag{15}$$

where $d_A$, $d_B$, and $d_C$ are the three-phase duty cycle, respectively.

**Table 2.** Duty cycle assignment.

| sector | Phase A | Phase B | Phase C |
|---|---|---|---|
| I | $d_A = d_x$ | $d_B = d_y$ | $d_C = d_0$ |
| II | $d_A = d_0$ | $d_B = d_x$ | $d_C = d_y$ |
| III | $d_A = d_y$ | $d_B = d_0$ | $d_C = d_x$ |

### 4.3. The Proof of Optimal Duty Cycle

To prove that the calculated duty cycle according to (12) is optimal, find the second-order partial derivative of the duty cycle for (7), and (16) is obtained.

$$\begin{cases} \dfrac{\partial^2 g}{\partial d_{mi}^2} = 2u_{mdi}^2 + 2u_{mqi}^2 = X \\ \dfrac{\partial^2 g}{\partial d_{mi} \partial d_{ni}} = 2u_{mdi}u_{ndi} + 2u_{mqi}u_{nqi} = Y \\ \dfrac{\partial^2 g}{\partial d_{ni}^2} = 2u_{ndi}^2 + 2u_{nqi}^2 = Z \end{cases} \tag{16}$$

According to (16), Equation (17) can be obtained as follows:

$$XZ - Y^2 = 4\left(u_{mdi}u_{nqi} - u_{ndi}u_{mqi}\right)^2 \tag{17}$$

Because $X > 0$, $XZ - Y^2 > 0$, the cost function takes a minimum value at (12). Since the squared cost function of the voltage error is constructed to minimize the cost function under the action of (12), the predicted voltage vector is closest to the reference voltage vector.

### 4.4. IMO Design

In (6), the reference voltage vector obtained by the deadbeat principle is designed according to the nominal parameters of the motor, but the motor parameters are time-varying during actual operation. If the disturbance caused by parameter mismatch is not compensated, the accuracy of the calculated reference voltage will be degraded.

The voltage equation considering parameter mismatch is expressed as follows:

$$u_d = \left(L_s + \Delta L_s\right)\frac{di_d}{dt} + \left(R_s + \Delta R_s\right)i_d - \left(L_s + \Delta L_s\right)\omega_e i_q \tag{18}$$

$$u_q = \left(L_s + \Delta L_s\right)\frac{di_q}{dt} + \left(R_s + \Delta R_s\right)i_q + \left(L_s + \Delta L_s\right)\omega_e i_d + \left(\psi_f + \Delta\psi_f\right)\omega_e \tag{19}$$

where $L_s$, $R_s$, and $\psi_f$ are the nominal parameters of the motor. $\Delta L_s = L_{s0} - L_s$, $\Delta R_s = R_{s0} - R_s$, $\Delta\psi_f = \psi_{f0} - \psi_f$. $L_{s0}$, $R_{s0}$, and $\psi_{f0}$ are the actual parameters of the motor.

From (18) and (19), all disturbances are extracted, then the disturbances $f_d$ and $f_q$ are expressed as follows:

$$\begin{cases} f_d = \Delta L_s\dfrac{di_d}{dt} + \Delta R_s i_d - \Delta L_s\omega_e i_q \\ f_q = \Delta L_s\dfrac{di_q}{dt} + \Delta R_s i_q + \Delta L_s\omega_e i_d + \Delta\psi_f\omega_e \end{cases} \tag{20}$$

The state equations of (18) and (19) are expressed as follows:

$$\dot{x} = Ax + B(u - f) \tag{21}$$

where $x = \begin{bmatrix} i_d \\ i_q \end{bmatrix}$, $u = \begin{bmatrix} u_d \\ u_q - \omega_e\psi_f \end{bmatrix}$, $A = \begin{bmatrix} -\frac{R_s}{L_s} & \omega_e \\ -\omega_e & -\frac{R_s}{L_s} \end{bmatrix}$, $B = \begin{bmatrix} \frac{1}{L_s} & 0 \\ 0 & \frac{1}{L_s} \end{bmatrix}$, $f = \begin{bmatrix} f_d \\ f_q \end{bmatrix}$.

The state observation equation obtained according to (21) is expressed as follows:

$$\dot{\hat{x}} = A\hat{x} + B\left(u - \hat{f}\right) \tag{22}$$

where $\hat{x}$ and $\hat{f}$ are the estimated values of state variables $x$ and $f$.

From (21) and (22), the error state equation is as follows:

$$\dot{\tilde{x}} = A\tilde{x} + B\tilde{f} \tag{23}$$

where $\tilde{x} = x - \hat{x}$, $\tilde{f} = f - \hat{f}$.

Taking the $d$-axis as an example, a new state equation is established as:

$$\begin{cases} \dot{\tilde{x}}_d = a\tilde{x}_d + b\tilde{d} \\ y = \tilde{x}_d \end{cases} \tag{24}$$

where $\tilde{x}_d = x_d - \hat{x}_d$, $x_d = i_d - \hat{i}_d$, $a = -\frac{R_s}{L_s}$, $b = \frac{1}{L_s}$, $\tilde{d} = f_d - \hat{f}_d$.

According to the internal model principle, it can be assumed that the input is 0, and $\tilde{d}$ is the control variable to be designed. The tracking error of (24) is as follows:

$$\begin{cases} e = 0 - y \\ \dot{e} = -\dot{y} = -\dot{\tilde{x}}_d \end{cases} \tag{25}$$

By introducing two state variables $z_1$ and $z_2$ such that $z_1 = \dot{\tilde{x}}_d$ and $z_2 = \dot{\tilde{d}}$, a new state equation can be obtained as follows:

$$\dot{z}_1 = \ddot{\tilde{x}}_d = az_1 + bz_2 \tag{26}$$

According to (25) and (26), the augmented matrix equation can be formed as follows:

$$\dot{z} = A_0 z + B_0 z_2 \tag{27}$$

where $A_0 = \begin{bmatrix} 0 & -1 \\ 0 & a \end{bmatrix}$, $B_0 = \begin{bmatrix} 0 \\ b \end{bmatrix}$, $z = \begin{bmatrix} e \\ z_1 \end{bmatrix}$.

$rank = \begin{bmatrix} B_0 & A_0 B_0 \end{bmatrix} = 2$, matrix is full rank, so the corresponding system of (27) is controllable. According to the principle of state feedback, state feedback control can be implemented. Let $z_2 = kz$, $k = \begin{bmatrix} k_1 & k_2 \end{bmatrix}$. By choosing $k$ reasonably, the system is asymptotically stable. From (25) and (27), the control variable $z_2$ can be obtained as:

$$z_2 = \dot{\tilde{d}} = k_1 e + k_2 z_1 = -k_1 \tilde{x}_d + k_2 \dot{\tilde{x}}_d \tag{28}$$

Since the sampling period $T_s$ is small enough, it can be considered that $\dot{d}$ is 0, then (28) can be expressed as:

$$\dot{\tilde{d}} = k_1 \tilde{x}_d - k_2 \dot{\tilde{x}}_d \tag{29}$$

The state feedback is formed by (27), and its closed-loop system matrix is $A_0 - B_0 k$. Then its characteristic equation is as follows:

$$\det\left[sI - (A_0 - B_0 k)\right] = s^2 - (a - k_2 b)\, s - k_1 b \tag{30}$$

Assuming the IMO closed-loop poles to be $\lambda_1$ and $\lambda_2$, then $k_1 = -\lambda_1\lambda_2/b$ and $k_2 = (a - \lambda_1 - \lambda_2)/b$ can be obtained, $k_1 < 0$, $k_2 > \frac{a}{b}$. The closed-loop poles $\lambda_1$ and $\lambda_2$ are located in the negative semi-axis, and the control system is in a stable state. By optimizing the parameters $k_1$ and $k_2$, and reasonably configuring the feedback matrix $A_0 - B_0 k$, the control law of IMO is determined. Under the action of (29), the system enters the steady state, and $z$ approaches 0. Then the corresponding state variables $e$ and $z_1$ tend to 0, and the uncertainty $\tilde{d}$ must also tend to 0, so that the estimated disturbance value is equal to the actual disturbance value. IMO estimates the changes of motor parameters and compensates the caused disturbance into the voltage equation, which can effectively reduce the current static error caused by the disturbance of motor parameters.

The analysis of the $q$-axis IMO is the same as that of the $d$-axis. The $d$-axis and $q$-axis IMO equations are expressed as:

$$\begin{cases} \dot{\hat{i}}_d = -\dfrac{R_s}{L_s}\hat{i}_d + \omega_e \hat{i}_q + \dfrac{1}{L_s}\left(u_d - \hat{f}_d\right) \\ \dot{\hat{f}}_d = k_1 \tilde{x}_d - k_2 \dot{\tilde{x}}_d \end{cases} \tag{31}$$

$$\begin{cases} \dot{\hat{i}}_q = -\dfrac{R_s}{L_s}\hat{i}_q - \omega_e \hat{i}_d + \dfrac{1}{L_s}\left(u_q - \omega_e \psi_f - \hat{f}_q\right) \\ \dot{\hat{f}}_q = k_3 \tilde{x}_q - k_4 \dot{\tilde{x}}_q \end{cases} \tag{32}$$

where $x_q = i_q - \hat{i}_q$, $k_3$, and $k_4$ are the feedback matrix gain.

The block diagrams of the $d$-axis and $q$-axis internal mode observers are shown in Figs. 7 and 8.

The ODC-MPCC strategy uses only 3 active voltage vectors, with a lower number of predictions. IMO estimates disturbance caused by the changes in motor parameters and performs feedforward compensation on the voltage equation, to reduce the current static error in the parameter mismatch. The overall flowchart of the algorithm is shown in Fig. 9.

## 5. EXPERIMENTAL VERIFICATION

To verify the effectiveness of the proposed strategy, first, a comparative experiment is performed on DV-MPCC and ODC-MPCC, and then, a comparative experiment is performed on ODC-MPCC with and without IMO. Experiments are conducted on an RT-LAB (OP5600) platform, and the system

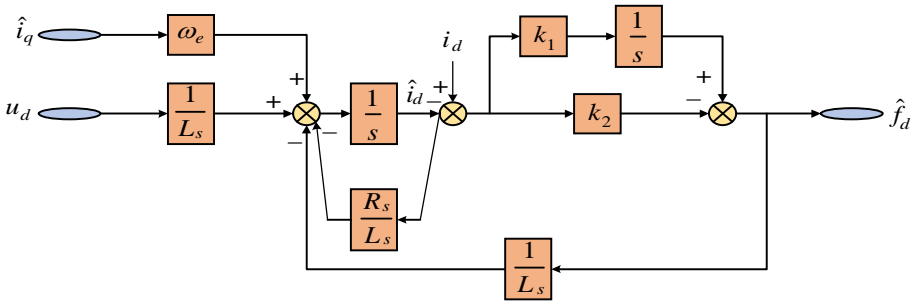


**Figure 7.** Structural block diagram of $d$-axis IMO.

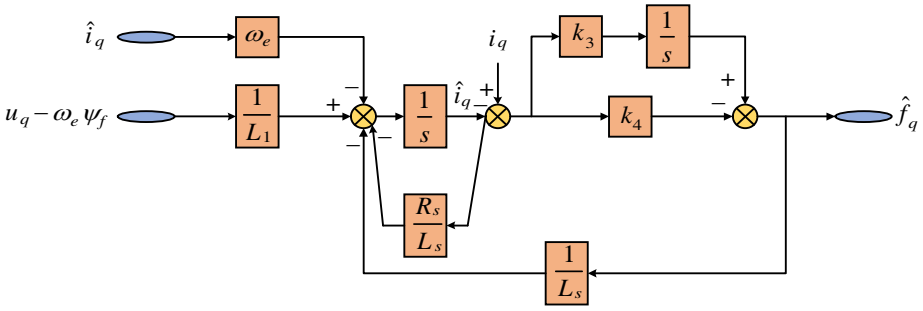


**Figure 8.** Structural block diagram of $q$-axis IMO.

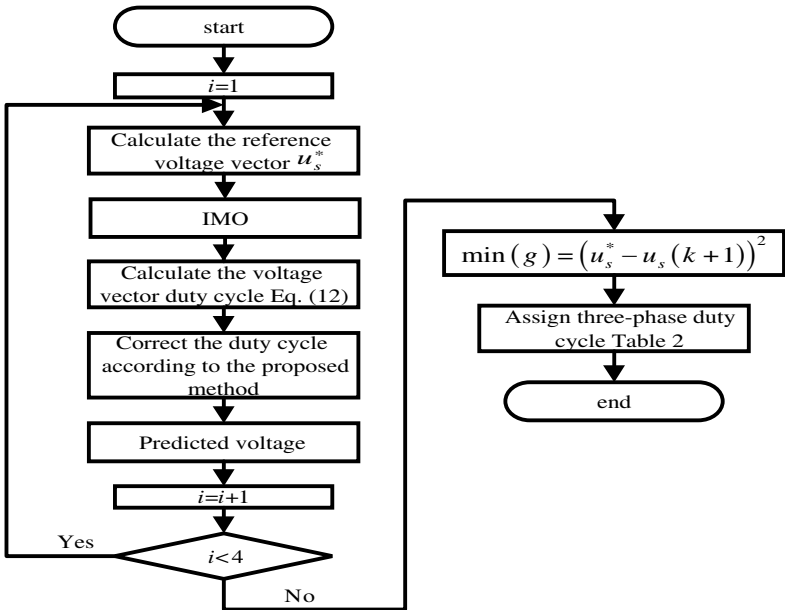


**Figure 9.** Flowchart of the IMO+ODC-MPCC.

is shown in Fig. 10. The Simulink model is downloaded to OP5600 to realize hardware in the loop simulation experiment (HLSE). The controller adopts TMS32F2812, and the inverter and PMSM are constructed by RT-LAB. Both strategies operate with the same motor parameters and discrete integral anti-saturation PI parameters ($k_p$ = 2.7, $k_i$ = 40), both with a sampling frequency of 10 kHz. The motor parameters are shown in Table 3.

Figure 11 shows the dynamic performance of the motor for variable speed and load torque. For DV-MPCC, the times required for no-load start operation to rated speed of 3000 r/min and reduction

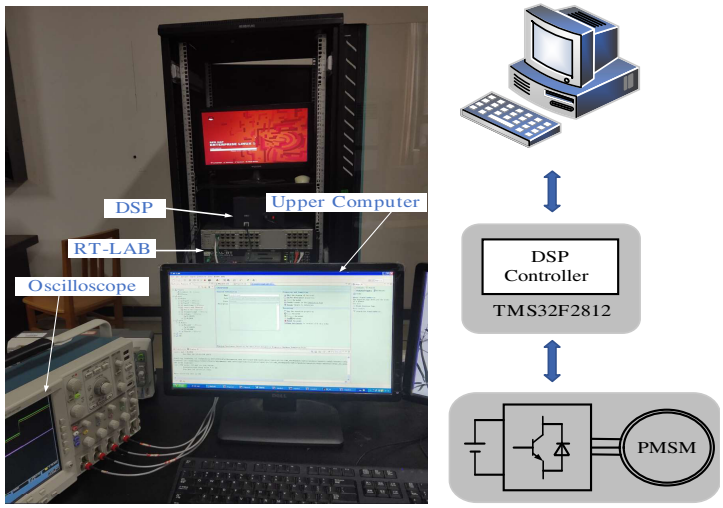


(a) (b)

**Figure 10.** RT-LAB semi-physical experimental platform. (a) Semi-physical composition. (b) System-in-the-loop configuration.

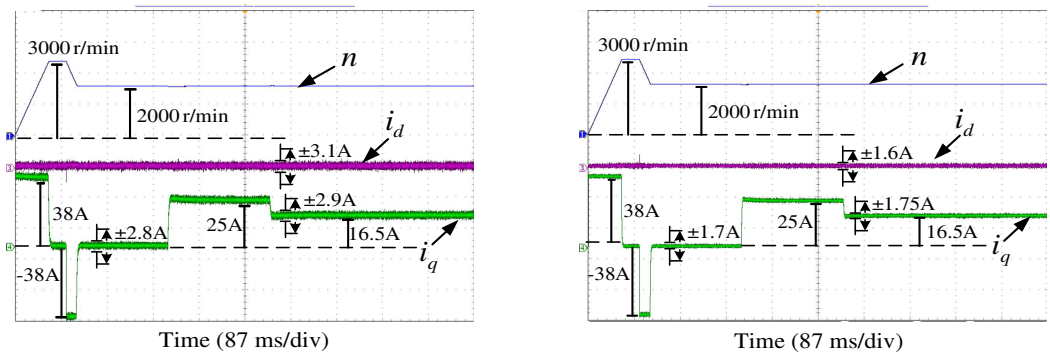


(a) DV-MPCC (b) ODC-MPCC

**Figure 11.** Motor speed and current curves for variable speed and load torque.

to 2000 r/min at 0.1 s are 0.069 s and 0.028 s, respectively. The load torque is increased to 15 N · m at 0.3 s, decreased from 15 N · m to 10 N · m at 0.5 s, and the speed recovery times are 0.072 s and 0.053 s, respectively. In the same case, for ODC-MPCC, the required times are 0.067 s, 0.023 s, 0.056 s, and 0.049 s, respectively. The speed and current of both strategies are essentially free of overshoot and static error. The dynamic performance of ODC-MPCC is slightly better, but the current ripple is significantly reduced.

Figure 12 illustrates the steady-state current waveform at 500 r/min and 5 N · m load torques. The current ripples $\Delta i_d$ and $\Delta i_q$ are calculated by (33), and the results are shown in Table 4. The data show that $\Delta i_d$ and $\Delta i_q$ of ODC-MPCC are reduced by 61.12% and 37.42%, respectively. Meanwhile, Fig. 12 shows that the stator current waveform is better for ODC-MPCC. The proposed strategy improves the steady-state performance of the motor.

$$\begin{cases} \Delta i_d = \sqrt{\dfrac{1}{N}\displaystyle\sum_{n=1}^{N}\left(i_d\left(n\right) - i_{d-ave}\right)^2} \\ \Delta i_q = \sqrt{\dfrac{1}{N}\displaystyle\sum_{n=1}^{N}\left(i_q\left(n\right) - i_{q-ave}\right)^2} \end{cases} \tag{33}$$

**Table 3.** PMSM parameters.

| Parameter | Value | Unit |
|---|---|---|
| Number of pole pairs | 4 | |
| Stator resistance | 0.15 | Ω |
| Stator inductance | 1.625 | mH |
| Permanent magnet flux | 0.1 | Wb |
| Moment of inertia | 4.78 | $g \cdot cm^2$ |
| Rated power | 4.5 | kW |
| Rated speed | 3000 | r/min |
| Rated torque | 15 | $N \cdot m$ |
| Rated voltage | 300 | V |
| peak current | 22.5 | A |
| peak torque | 38.18 | $N \cdot m$ |

**Table 4.** Steady-state current ripple.

| Strategy | condition | $\Delta i_d$/A | $\Delta i_q$/A |
|---|---|---|---|
| DV-MPCC | 500 r/min, 5 $N \cdot m$ | 0.1824 | 0.2047 |
| ODC-MPCC | | 0.0708 | 0.1281 |

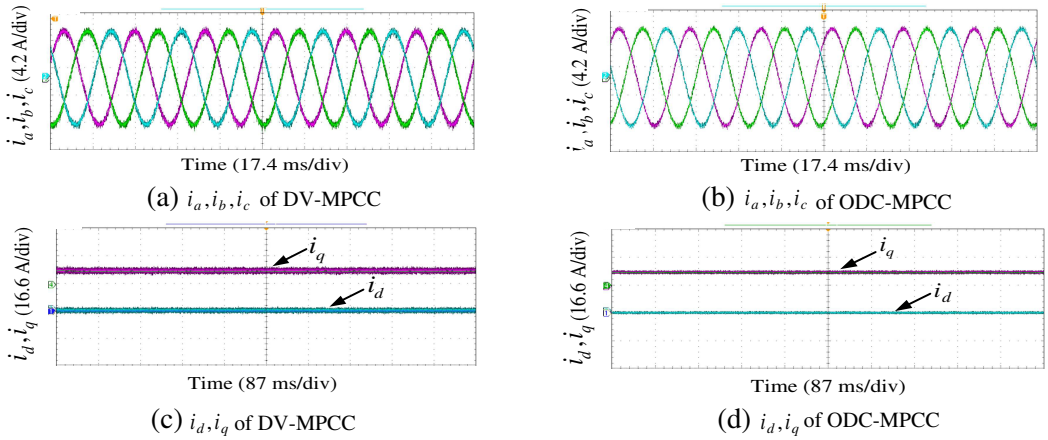


**Figure 12.** Steady-state current waveforms at 1000 r/min and 10 $N \cdot m$.

where $N$ is the number of samples; $i_{d-ave}$ and $i_{q-ave}$ are the average values of the $d$-$q$ axis currents; $i_d(n)$ and $i_q(n)$ are the $d$-$q$ axis currents at the constant $n$.

At 1000 r/min and 10 $N \cdot m$ load torques, $i_a$ and FFT analysis are shown in Fig. 13. It can be seen from Fig. 13 that the phase current harmonic of ODC-MPCC is significantly smaller than that of DV-MPCC, and compared with the DV-MPCC, the total harmonic distortion (THD) of $i_a$ is 6.30% and 3.17%, respectively. The results show that ODC-MPCC can effectively reduce phase current harmonics and improve waveform quality.

To illustrate more effectively that current ripple can be reduced using ODC-MPCC, the current ripple at 400 r/min, 800 r/min, 1200 r/min, 1600 r/min, 2000 r/min 2400 r/min, and 2800 r/min at no-load is calculated, also by (33). The calculation result is shown in Fig. 14. The results show that the ODC-MPCC has the smallest $d$-$q$ axis currents ripple in the full speed range. Taking the current ripple

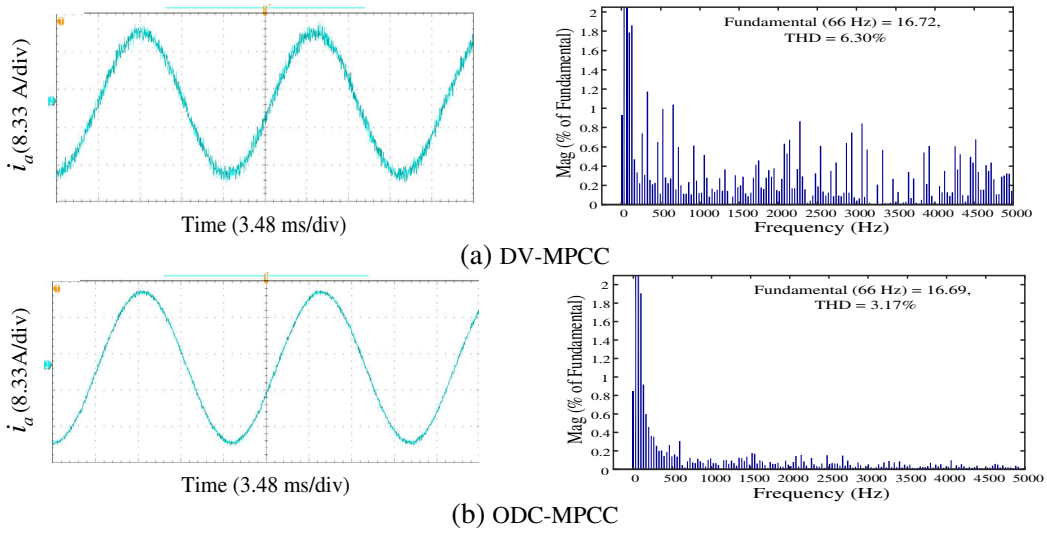


**Figure 13.** Phase current $i_a$ waveform and FFT analysis.

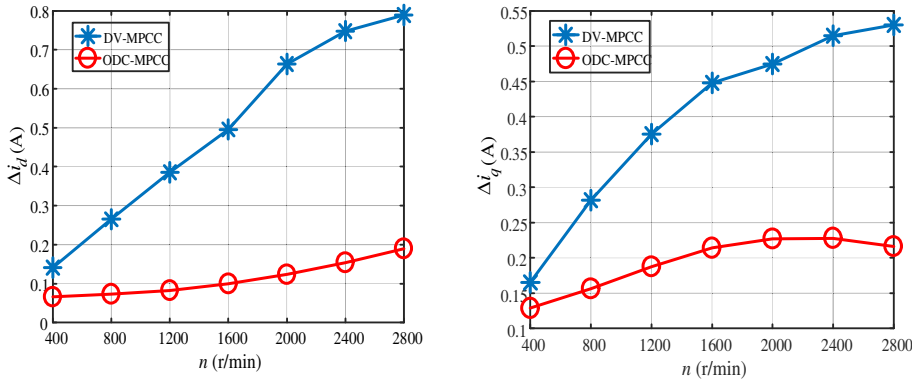


**Figure 14.** Current ripple at different speeds with no load.

at 2400 r/min as an example for analysis, the $\Delta i_d$ and $\Delta i_q$ of ODC-MPCC DV-MPCC and DV-MPCC are 0.154 A and 0.228 A, 0.748 A and 0.515 A, respectively, and $\Delta i_d$ is decreased by 7941% and $\Delta i_q$ by 55.73% compared with DV-MPCC.

The voltage vector distributions of the two strategies at 500 r/min and 1000 r/min no-load operation are shown in Fig. 15. It can be seen that the output voltage vector of DV-MPCC is only on the 6 active voltage vector axes, while ODC-MPCC is the whole circle. Therefore, the larger the voltage range is covered by the control strategy proposed, the better the control effect is, which can effectively reduce the current ripple. The simulation results are consistent with the theoretical analysis. At the same speed and load torque, the average voltage utilization is increased by 16.7%.

Using MATLAB built-in tic and toc functions, the time used by the DSP core algorithms in two strategies is tested iteratively to obtain the average value. The test results are shown in Table 5. The results show that the execution times of DV-MPCC and ODC-MPCC are 0.875 s and 0.759 s, respectively, and the execution time of ODC-MPCC is reduced by 0.116 s. Because ODC-MPCC has less prediction times and reduces the execution time of the algorithm, the strategy is conducive to practical operation.

In [26], the influences of motor parameters variation on the current are introduced in detail and will not be repeated here. Since the motor parameters cannot be freely modified during the experiment, the changes of motor parameters are simulated by changing the controller parameters. Fig. 16 shows

**Table 5.** The number of predictions and the execution time of the core algorithm for the two strategies.

| Strategy | DV-MPCC | ODC-MPCC |
|---|---|---|
| Number of predictions | 6 | 3 |
| Execution time | 0.875 s | 0.759 s |

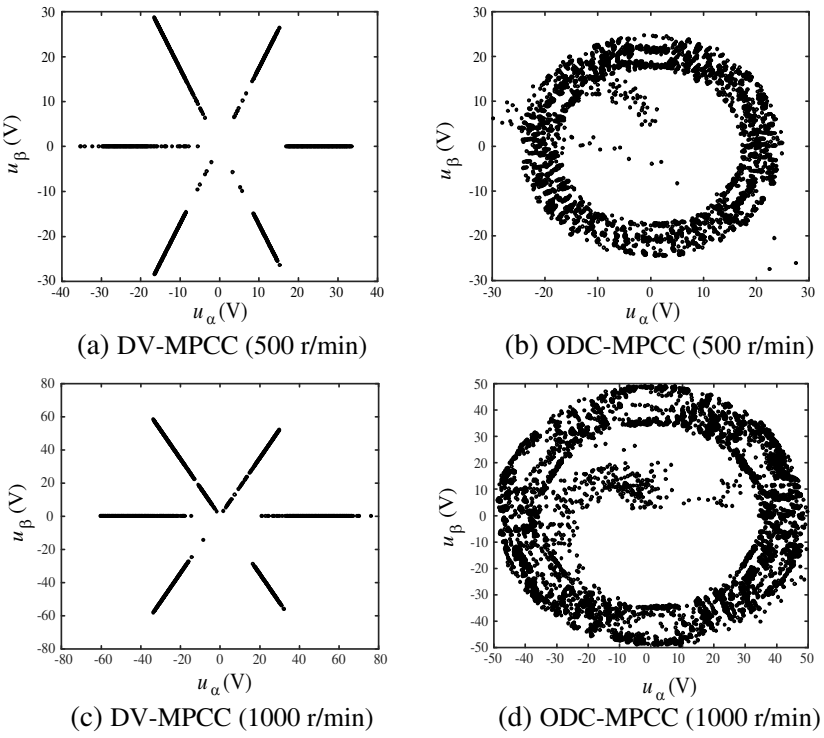


(a) DV-MPCC (500 r/min) (b) ODC-MPCC (500 r/min)

(c) DV-MPCC (1000 r/min) (d) ODC-MPCC (1000 r/min)

**Figure 15.** The voltage vector distribution diagrams of two strategies at 500 r/min and 1000 r/min no-load operation.

the steady-state current and disturbance estimation with and without IMO for the ODC-MPCC at 2000 r/min and 15 N · m load torques. Experimental results show that the inductance mismatch has a significant influence on the $d$-axis current; the flux linkage mismatch has a great influence on the $q$-axis current; and the resistance mismatch has little effect on the $d$-$q$ axis currents, which is consistent with the conclusion of [26]. IMO+ODC-MPCC adds disturbance compensation, which has strong robustness to $R_s$, $L_s$, and $\psi_f$ interference. From Figs. 15(d), (e), and (f), it is seen that the static error of the $d$-$q$ axis current is very small, indicating that IMO provides accurate disturbance compensation for ODC-MPCC. It is not difficult to find the interference $\hat{f}_d$ and $\hat{f}_q$ observed by IMO, which adapts well to parameter changes and compensates for mismatched models accordingly. The static error formula for parameter mismatch is (34). For the ODC-MPCC with or without IMO, the static error calculation results are shown in Table 6. The results show that the IMO+ODC-MPCC strategy reduces the current static error under parameters mismatch and improves the steady-state performance of the control system.

$$\begin{cases} \sigma_{id} = \dfrac{1}{\mathrm{N}} \displaystyle\sum_{n=1}^{N} \left| i_d(n) - i_d^*(n) \right| \\ \sigma_{iq} = \dfrac{1}{\mathrm{N}} \displaystyle\sum_{n=1}^{N} \left| i_q(n) - i_q^*(n) \right| \end{cases} \tag{34}$$

where $i_d^*(n)$ and $i_q^*(n)$ are the $d$-$q$ axis currents reference at the constant $n$, respectively.

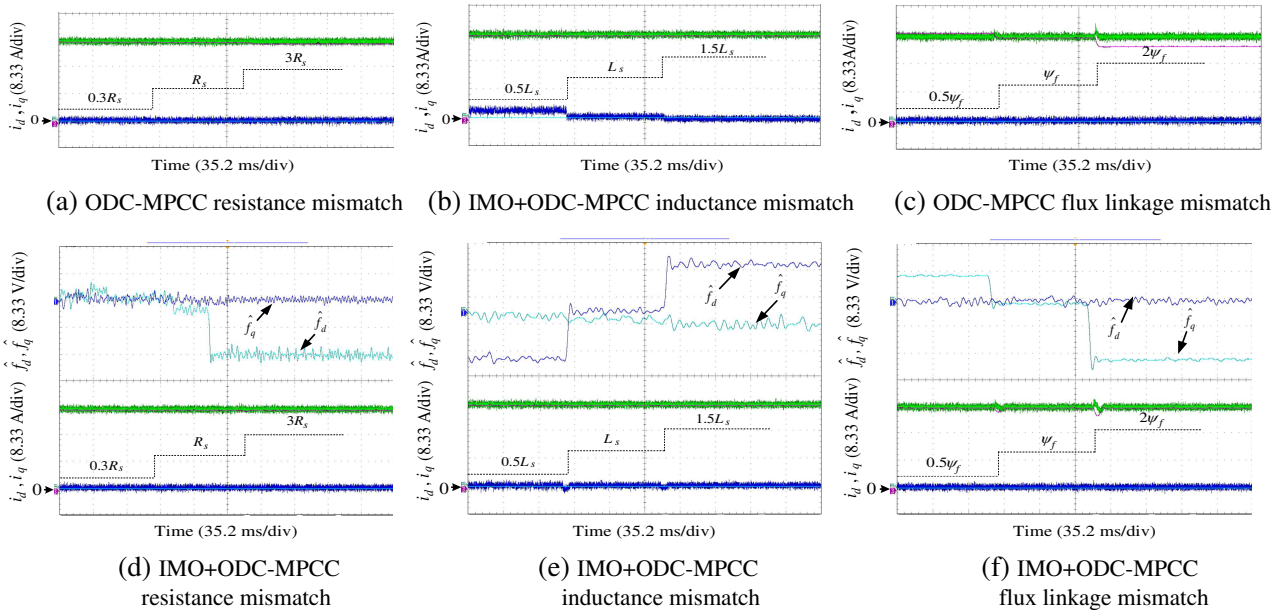


(a) ODC-MPCC resistance mismatch (b) IMO+ODC-MPCC inductance mismatch (c) ODC-MPCC flux linkage mismatch

(d) IMO+ODC-MPCC resistance mismatch (e) IMO+ODC-MPCC inductance mismatch (f) IMO+ODC-MPCC flux linkage mismatch

**Figure 16.** Current and interference waveforms for ODC-MPCC strategies with and without IMO.

**Table 6.** Current static error of ODC-MPCC with or without IMO under parameters mismatch.

| Strategy | parameters mismatch | $\sigma_{id}$/A | $\sigma_{iq}$/A |
|---|---|---|---|
| ODC-MPCC | $0.3R_s \rightarrow R_s \rightarrow 3R_s$ | 0.162 | 0.283 |
| IMO+ODC-MPCC | $0.3R_s \rightarrow R_s \rightarrow 3R_s$ | 0.148 | 0.263 |
| ODC-MPCC | $0.5L_s \rightarrow L_s \rightarrow 1.5L_s$ | 0.507 | 0.286 |
| IMO+ODC-MPCC | $0.5L_s \rightarrow L_s \rightarrow 1.5L_s$ | 0.158 | 0.267 |
| ODC-MPCC | $0.5\psi_f \rightarrow \psi_f \rightarrow 2\psi_f$ | 0.177 | 1.089 |
| IMO+ODC-MPCC | $0.5\psi_f \rightarrow \psi_f \rightarrow 2\psi_f$ | 0.149 | 0.266 |

## 6. CONCLUSION

In this paper, an ODC-MPCC based on IMO is proposed. The following conclusions are drawn from theoretical analysis and experiments.

(1) The dynamic performance of ODC-MPCC is slightly better than that of DV-MPCC, but ODC-MPCC has better steady-state performance and can effectively reduce current ripple and phase current harmonics.

(2) The number of predictions of ODC-MPCC is only 3, so the algorithm is more efficient.

(3) The designed IMO can accurately estimate the system disturbance under parameter mismatch and compensate them feedforward into voltage equation. The current static error is reduced, and the steady-state performance is improved.

## ACKNOWLEDGMENT

This work was supported by the National Natural Science Foundation of China under Grant Number 51907061 and Educational Commission of Hunan Province of China under Grant Number 21B0552.

## REFERENCES


1. Sun, X., Z. Shi, Y. Cai, G. Lei, Y. Guo, and J. Zhu, "Driving-cycle-oriented design optimization of a permanent magnet hub motor drive system for a four-wheel-drive electric vehicle," *IEEE Transactions on Transportation Electrification*, Vol. 6, No. 3, 1115–1125, Sept. 2020, doi: 10.1109/TTE.2020.3009396.
2. Quang, N. H., N. P. Quang, D. P. Nam, et al., "Multi parametric model predictive control based on Laguerre model for permanent magnet linear synchronous motors," *International Journal of Electrical and Computer Engineering (IJECE)*, Vol. 9, No. 2, 1067–1077, 2019.
3. Zhu, Z., Y. Tian, X. Wang, L. Li, X. Luan, and Y. Gao, "Fusion predictive control based on uncertain algorithm for PMSM of brake-by-wire system," *IEEE Transactions on Transportation Electrification*, Vol. 7, No. 4, 2645–2657, Dec. 2021, doi: 10.1109/TTE.2021.3065249.
4. Zhang, Y., J. Jin, and L. Huang, "Model-free predictive current control of PMSM drives based on extended state observer using ultralocal model," *IEEE Transactions on Industrial Electronics*, Vol. 68, No. 2, 993–1003, Feb. 2021, doi: 10.1109/TIE.2020.2970660.
5. Wendel, S., A. Dietz, and R. Kennel, "FPGA based finite-set model predictive current control for small PMSM drives with efficient resource streaming," *2017 IEEE International Symposium on Predictive Control of Electrical Drives and Power Electronics (PRECEDE)*, 66–71, 2017, doi: 10.1109/PRECEDE.2017.8071270.
6. Petkar, S. G., K. Eshwar, and V. K. Thippiripati, "A modified model predictive current control of permanent magnet synchronous motor drive," *IEEE Transactions on Industrial Electronics*, Vol. 68, No. 2, 1025–1034, Feb. 2021, doi: 10.1109/TIE.2020.2970671.
7. Xu, Y., B. Zhang, and Q. Zhou, "Predictive current control of permanent magnet synchronous motor with dual vector model," *Journal of Electrotechnical Technology*, Vol. 32, No. 20, 222–230, Chinese Journals, 2017.
8. Lin, H. and W. Song, "Three-vector model predictive current control of permanent magnet synchronous motor based on SVM," *2019 IEEE International Symposium on Predictive Control of Electrical Drives and Power Electronics (PRECEDE)*, 1–6, 2019, doi: 10.1109/PRECEDE.2019.8753364.
9. Lin, C., T. Liu, J. Yu, L. Fu, and C. Hsiao, "Model-free predictive current control for interior permanent-magnet synchronous motor drives based on current difference detection technique," *IEEE Transactions on Industrial Electronics*, Vol. 61, No. 2, 667–681, Feb. 2014, doi: 10.1109/TIE.2013.2253065.
10. Shao, M., Y. Deng, H. Li, J. Liu, and Q. Fei, "Robust speed control for permanent magnet synchronous motors using a generalized predictive controller with a high-order terminal sliding-mode observer," *IEEE Access*, Vol. 7, 121540–121551, 2019, doi: 10.1109/ACCESS.2019.2937535.
11. Romero, J. G., R. Ortega, Z. Han, et al., "An adaptive flux observer for the permanent magnet synchronous motor," *International Journal of Adaptive Control and Signal Processing*, Vol. 30, No. 3, 473–487, 2016.
12. Shi, T., Y. Yan, Z. Zhou, M. Xiao, and C. Xia, "Linear quadratic regulator control for PMSM drive systems using nonlinear disturbance observer," *IEEE Transactions on Power Electronics*, Vol. 35, No. 5, 5093–5101, May 2020, doi: 10.1109/TPEL.2019.2947259.
13. Li, G., W. Xu, J. Zhao, et al., "Precise robust adaptive dynamic surface control of permanent magnet synchronous motor based on extended state observer," *IET Science, Measurement & Technology*, Vol. 11, No. 3, 590–599, May 2017.
14. He, L., F. Wang, J. Wang, and J. Rodríguez, "Zynq implemented luenberger disturbance observer based predictive control scheme for PMSM drives," *IEEE Transactions on Power Electronics*, Vol. 35, No. 2, 1770–1778, Feb. 2020, doi: 10.1109/TPEL.2019.2920439.
15. Gabbi, T. S., H. Abilio Grundling, and R. Padilha Vieira, "Sliding mode current control based on disturbance observer applied to permanent magnet synchronous motor," *2015 IEEE 13th Brazilian Power Electronics Conference and 1st Southern Power Electronics Conference (COBEP/SPEC)*, 1–6, 2015, doi: 10.1109/COBEP.2015.7420038.

16. Shen, Y., Q. Xu, Y. Ma, and Y. Zou, "Application of an improved ADRC controller based on the double closed loop dynamic disturbance compensation in PMSM," *2018 21st International Conference on Electrical Machines and Systems (ICEMS)*, 435–440, 2018, doi: 10.23919/ICEMS.2018.8549467.
17. Niu, S., Y. Luo, W. Fu, and X. Zhang, "Robust model predictive control for a three-phase PMSM motor with improved control precision," *IEEE Transactions on Industrial Electronics*, Vol. 68, No. 1, 838–849, Jan. 2021, doi: 10.1109/TIE.2020.3013753.
18. Niu, F., W. Xiao, H. Shao, et al., "Current prediction error reduction method of predictive current control for permanent magnet synchronous motors," *IEEE Access*, Vol. 8, 124288–124296, 2020, doi: 10.1109/ACCESS.2020.3006132.
19. Wang, G., M. Yang, L. Niu, et al., "Current static error elimination algorithm for current predictive control of permanent magnet synchronous motor," *Chinese Journal of Electrical Engineering*, Vol. 35, No. 10, 2544–2551, Chinese Journals, 2015.
20. Liu, G., L. Chen, W. Zhao, Y. Jiang, and L. Qu, "Internal model control of permanent magnet synchronous motor using support vector machine generalized inverse," *IEEE Transactions on Industrial Informatics*, Vol. 9, No. 2, 890–898, May 2013, doi: 10.1109/TII.2012.2222652.
21. Zhang, R., Z. Yin, N. Du, J. Liu, and X. Tong, "Robust adaptive current control of a 1.2-MW direct-drive PMSM for traction drives based on internal model control with disturbance observer," *IEEE Transactions on Transportation Electrification*, Vol. 7, No. 3, 1466–1481, Sept. 2021, doi: 10.1109/TTE.2021.3058012.
22. Li, S. and H. Gu, "Fuzzy adaptive internal model control schemes for PMSM speed-regulation system," *IEEE Transactions on Industrial Informatics*, Vol. 8, No. 4, 767–779, Nov. 2012, doi: 10.1109/TII.2012.2205581.
23. Chen, M., F. Wang, L. He, D. Ke, K. Zuo, and J. Rodriguez, "Predictive current control of permanent magnet synchronous motor based on an adaptive internal model observer," *2020 IEEE 9th International Power Electronics and Motion Control Conference (IPEMC2020-ECCE Asia)*, 2567–2571, 2020, doi: 10.1109/IPEMC-ECCEAsia48364.2020.9368203.
24. Yan, L., M. Dou, Z. Hua, H. Zhang, and J. Yang, "Optimal duty cycle model predictive current control of high-altitude ventilator induction motor with extended minimum stator current operation," *IEEE Transactions on Power Electronics*, Vol. 33, No. 8, 7240–7251, Aug. 2018, doi: 10.1109/TPEL.2017.2759906.
25. Zhou, Z., C. Xia, Y. Yan, Z. Wang, and T. Shi, "TorquE RIPPLE MINIMIZATION OF PREDICTIVE TORQUE CONTROL FOR PMSM with extended control set," *IEEE Transactions on Industrial Electronics*, Vol. 64, No. 9, 6930–6939, Sept. 2017, doi: 10.1109/TIE.2017.2686320.
26. Liu, X., L. Zhou, J. Wang, X. Gao, Z. Li, and Z. Zhang, "Robust predictive current control of permanent-magnet synchronous motors with newly designed cost function," *IEEE Transactions on Power Electronics*, Vol. 35, No. 10, 10778–10788, Oct. 2020, doi: 10.1109/TPEL.2020.2980930.